Effect of computational methodology on the conformational dynamics of the protein photosensor LOV1 from Chlamydomonas reinhardtii

ARTICLE *in* JOURNAL OF CHEMICAL BIOLOGY · OCTOBER 2011

DOI: 10.1007/s12154-011-0060-z · Source: PubMed

3 AUTHORS, INCLUDING:

Emanuel Peter
University of Lugano
20 PUBLICATIONS **90** CITATIONS
SEE PROFILE

Bernhard Dick
Universität Regensburg
143 PUBLICATIONS **2,652** CITATIONS
SEE PROFILE

J Chem Biol (2011) 4:167–184
DOI 10.1007/s12154-011-0060-z

ORIGINAL ARTICLE

Effect of computational methodology on the conformational dynamics of the protein photosensor LOV1 from *Chlamydomonas reinhardtii*

Emanuel Peter · Bernhard Dick · Stephan A. Baeurle

Received: 7 December 2010 / Accepted: 17 February 2011 / Published online: 11 March 2011

Abstract LOV domains are the light-sensitive protein domains of plant phototropins and bacteria. They photochemically form a covalent bond between a flavin mononucleotide (FMN) chromophore and a cysteine, attached to the apo-protein, upon irradiation with blue light, which triggers a signal in the adjacent kinase. Although their signaling state has been well characterized through experimental means, their signal transduction pathway as well as dark-state activity are generally only poorly understood. Here we show results from molecular dynamics simulations where we investigated the effect of thermostating and long-range electrostatics on the solution structure and dynamical behavior of the wild-type LOV1 domain from the green algae *Chlamydomonas reinhardtii* in the dark. We demonstrate that these computational issues can dramatically affect the conformational fluctuations of such protein domains by suppressing configurations far from equilibrium or destabilizing local configurations, leading to artificial changes of the protein secondary structure as well as the H-bond network formed by the amino acids and the FMN. By comparing our calculation results with recent experimental data, we show that the non-invasive thermostating strategy, where the protein solute is only indirectly coupled to the thermostat via the solvent, in conjunction with the particle-mesh Ewald technique, provides dark-state conformers, which are in consistency with experimental observations. Moreover, our calculations indicate that the LOV1 domains can alter the intersystem crossing rate and rate of adduct formation by adjusting the population distribution of these dark-state conformers. This might permit them to function as a modulator of the signal intensity under low light conditions.

Keywords Protein photosensor · Phototropin · Plant · Bacteria · LOV

Introduction

Phot proteins are blue-light photoreceptors found in higher plants as well as in microalgae. They regulate biological processes such as phototropic plant movement, chloroplast relocation, stomatal opening, rapid inhibition of stem growth, and gametogenesis [1–4]. They are composed of two light-oxygen-voltage (LOV) domains, each containing a non-covalently bound flavin mononucleotide (FMN) chromophore and a C-terminal kinase domain. Upon blue-light absorption, a covalent bond between the FMN chromophore and an adjacent reactive cysteine residue of the apo-protein is formed in the LOV domains (see Fig. 1). This subsequently mediates the activation of the kinase domain, which induces a signal in the organism via photoreceptor auto-phosphorylation [5]. A common feature of phot proteins is that the photochemical reactivity of LOV2 is required for the activation of the attached kinase domain. By contrast, the role of LOV1 is still unclear, although size exclusion chromatography in addition to small-angle X-ray scattering analysis suggests that this domain may be involved in photoreceptor dimerization [6, 7]. In several studies, it has been proposed that the LOV1

Electronic supplementary material The online version of this article (doi:10.1007/s12154-011-0060-z) contains supplementary material, which is available to authorized users.

E. Peter · B. Dick · S. A. Baeurle (✉)
Department of Chemistry and Pharmacy,
Institute of Physical and Theoretical Chemistry,
University of Regensburg,
93040 Regensburg, Germany
e-mail: stephan.baeurle@chemie.uni-regensburg.de

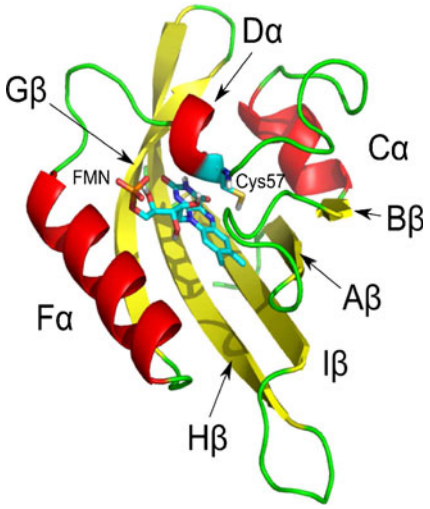

Fig. 1 Protein secondary structure of the wild-type LOV1 domain from *C. reinhardtii*, obtained by Fedorov et al. using X-ray diffraction [12] (MD starting structure)

domain might be responsible for regulating the lifetime and signal intensity of the LOV2 domain under low light conditions and in this way affect the phototropin activity [4, 8–10]. In the past decade, the primary photoreaction mechanism and the initial structural changes of the wild-type LOV domains, as well as related mutants, have been investigated in detail through experimental as well as theoretical means. However, despite tremendous efforts, still only little is known about their signal transduction pathway as well as dark-state activity on the molecular level.

To elucidate the photocycle, Kottke et al. [11] investigated the LOV1 domain of phot1 from *Chlamydomonas reinhardtii* with time-resolved absorption spectroscopy. They found that photoexcitation of the dark-state form of LOV1, designated as LOV1-447, causes transient bleaching and the formation of two spectrally similar red-shifted intermediates that can both be assigned to triplet states of the FMN. These triplet states decay with time constants of 800 ns and 4 μs with an efficiency of >90% into a blue-shifted intermediate, designated as LOV1-390, that can be correlated with the formation of a thio-adduct between the reactive cysteine residue (Cys57) of the apo-protein and the C4a atom on FMN (FMN–C4a). Then, the adduct state LOV1-390 reverts to the dark-state form in hundreds of seconds with a time constant being dependent on pH and salt concentration. Fedorov et al. [12] performed accurate measurements of the crystal structure of the LOV1 domain from the same species in the dark and illuminated state (resolution, 1.9 Å) and discovered two different dark-state conformers, populated with a probability distribution of 70%:30%. They concluded from their study that the conformers differ in the rotation around the C_α–C_β bond of the Cys57 residue, which may possess a different reactivity and could explain the occurrence of the two triplet states observed in the spectroscopic experiments of Kottke et al. [11]. Through Fourier-transformed infrared (FTIR) spectroscopy, Bednarz et al. [13] further established that in both conformers the thiol group is exposed to environments of different H-bonding strength and correlated the structural characteristics of the dark-state conformers with the decay kinetics of the respective triplet states. Schleicher et al. [14] studied the photo-induced triplet state and the photoreactivity of the FMN cofactor in wild-type LOV1 and LOV2 domains as well as in mutant LOV domains from *C. reinhardtii*, *Avena sativa*, and *Adiantum capillus-veneris* by time-resolved electron paramagnetic resonance and UV–visible spectroscopy at low temperatures ($T \leq 80$ K). They suggested that differences in the electronic structure of the FMN, as reflected by altered zero-field splitting parameters of the triplet state, can be correlated with changes in the amino acid composition of the binding pocket. In a multitude of subsequent experimental studies, it has been demonstrated that the photochemically induced signal of phototropin, initiated by adduct formation, is very different from that of other photoactive proteins where the photoreaction is initiated by photoisomerization, for example, in the case of the rhodopsins, photoactive yellow protein (PYP) and phytochrome. While the photoreactions of the latter proteins show only little temperature sensitivity, the phototropins show a highly temperature-dependent photoreaction and signal transduction pathway [15]. To investigate this aspect, Iwata et al. [16] compared the light-induced structural changes of the LOV1 and LOV2 domains of a phototropin from *Adiantum phytochrome3* (phy3) by means of UV–visible and FTIR spectroscopy in the temperature range from 77 to 295 K. They observed that the thiol group of the reactive cysteine residue forms an H-bond in phy3-LOV1, which is strengthened at low temperatures. They related this with the fact that no adduct formation takes place for phy3-LOV1 at 77 K, as revealed by UV–visible spectroscopy. A reduction of the occurrence of the adduct form was also observed for phy3–LOV2 at a low temperature [17], i.e., at 77 K, the yield of the adduct state of phy3–LOV2 decreased by an amount of 36% with regard to the yield at room temperature. Based on these experiments, Iwata et al. [16, 17] suggested that the presence of a non-reactive fraction of dark-state conformers at low temperature may originate from a local structural heterogeneity between the FMN and the reactive cysteine residue whose thiol group might form an H-bond with some surrounding amino acid sidechain, peptide carbonyl, or internal water molecule. In such a situation, the respective reaction centers may thus be too far from each other and could possess a mobility too low to form an adduct state. In a subsequent FTIR study, Sato et al. [15] observed dark-state conformers with different S–H

stretching frequencies and suggested that the micro-environment of the thiol group of the reactive cysteine residue determines the reactivity at low temperatures. Kennis et al. [18] investigated the molecular mechanism of signaling of the LOV2 domain with an additional α-helix, called the Jα-helix, of phot1 from *A. sativa* (AsLOV2-Jα) using FTIR spectroscopy. In this study, they characterized a newly isolated low-hydration intermediate that shows a downshift of high-frequency amide I signals and possibly corresponds to a loop tightening without large structural changes at the β-sheet or the Jα-helix. In addition, they reported a heterogeneity involving two different populations of FMN–C4=O conformers coexisting in the dark state and characterized by two different C4=O–carbonyl frequencies. They explained the occurrence of these two carbonyl frequencies by the presence of conformers with either a singly H-bonded or twice-H-bonded FMN–C4=O with the surrounding amino acids. According to their analysis, these conformers display slightly shifted absorption spectra and cause a splitting of the 475-nm band in the UV–visible spectra of the LOV domains at low temperature.

From the theoretical side, a major focus was put on the investigation of the primary steps of photoreaction and the initial structural changes after blue-light absorption of the photocycle. Fedorov et al. [12] performed first quantum chemical calculations with their crystal structure configurations, which provided information about the possible pathways of the photoreaction in the active site. They concluded from their study that the light-induced structural changes of the protein domain in the crystal are minor and mainly take place around the chromophore. Neiss and Saalfrank [19] performed ab initio quantum mechanical calculations to determine the electronic properties of several FMN-related model compounds in different charge and spin states. They deduced from their calculation results that the reaction pathway takes place via the triplet T1-state of the FMN and that the process of adduct formation involves rather intermediate radicals instead of ionic species. Dittrich et al. [20] studied the early steps of the photocycle by performing combined quantum mechanical/molecular mechanical (QM/MM) simulations of a complete LOV1 domain from *C. reinhardtii*. They investigated the electronic properties and initial structural changes that follow blue-light absorption and concluded from their calculation results that the pathway for cysteinyl–FMN adduct formation proceeds via a neutral radical state generated by H atom transfer from the reactive Cys57 residue to the FMN chromophore. In a later work, Freddolino et al. [21] investigated the structural changes, taking place at longer times after adduct formation, by performing molecular dynamics (MD) simulations with the LOV1 domain from *C. reinhardtii* and the LOV2 domain from *A. sativa*. To this end, they performed five independent 12-ns simulations with the light and dark states of both protein domains, revealing significant differences in how the LOV1 and LOV2 domains respond to photoactivation. Based on their calculation results, they proposed that LOV1 activation is caused by a change in the H-bond network between FMN chromophore and the surrounding apo-protein that destabilizes a highly conserved salt bridge, whereas LOV2 activation results from a change in flexibility of a set of protein loops. Neiss and Saalfrank [22] performed MD simulations with the dark and illuminated state of the LOV2 domain of *Adiantum capillus-veneris*. In accordance with the accurate X-ray diffraction measurements of Fedorov et al. [12] for the LOV1 domain from *C. reinhardtii*, they detected three dark-state conformers, which are populated with about equal probability and differ with respect to a rotation around the C_α–C_β bond of the reactive Cys57 residue. However, they found no clear changes in the structure or dynamics of the protein domain, which could be relevant for signal transduction after adduct formation, and suggested that the conformational behavior of the isolated LOV2 domain in the crystal should differ from the biologically active LOV2 in solution in its natural environment. Similar findings were also recently made for related photoactive proteins. Arai et al. [23] found that, for the putative signaling state of PYP, there are serious discrepancies between the crystal structure, obtained from time-resolved Laue diffraction analysis, and the solution structure, obtained from various spectroscopic studies. To explore the origin of such disagreements, they performed MD simulations with the PYP in the crystal and compared the results with those from MD simulations of the protein in solution. They found clear differences in the root mean square deviation when they relaxed the crystallographically determined structure of the protein in solution. Finally, Sato et al. [15] performed MD simulations in conjunction with a FTIR study on the LOV2 domain from *Adiantum neochrome 1* (neo1) and observed that multiple protein conformers can co-exist, differing in the heterogeneous environment of the reactive cysteine residue. They found that the conformers can thermally be converted into each other by conformational fluctuations at physiological temperatures. However, the effects of the calculation procedure, e.g., the thermostating and treatment of the long-range electrostatic interactions, on the solution structure and conformational fluctuations of the dark-state conformers have not been analyzed in these works.

In the present study, our goal is to investigate the influence of the calculation procedure on the solution structure and the conformational fluctuations of the wild-type LOV1 domain from the green algae *C. reinhardtii* in its monomeric and dimeric form. In particular, we consider the effect of different electrostatics and thermostating on the conformational heterogeneity of the dark-state conformers. The importance of electrostatics on influencing peptide or

small protein conformations has been demonstrated in several recent computer simulation studies. For example, the commonly used particle-mesh Ewald (PME) technique has been suspected to lead to a structural stabilization of the secondary structure [24–27], whereas the computationally cheap cutoff techniques have been found to result in a structural destabilization [28, 29]. Here we will test the reliability of these methods for treating large heterogeneous protein systems, typically containing a multitude of different length and time scales [30]. To this end, we will perform extensive long-time molecular dynamics simulations with the wild-type LOV1 domain from *C. reinhardtii* in the dark and compare the calculation results to data from recent experiments. Another major aspect will focus on the effect of the thermostating procedure on the protein secondary structure and conformational fluctuations of such photoactive protein domains. It has recently been demonstrated that the equilibrium as well as non-equilibrium conformational behavior of peptides and small proteins is very sensitive to the thermostating strategy [31]. We will show in the following discussions that these issues can significantly affect the conformational heterogeneity of the dark-state conformers of the LOV1 domain whose shift in population distribution might be relevant for adapting the functionality of the photosensor to different external conditions.

Our paper is organized in the following way. In "Methods", we review and discuss the most important long-range electrostatics and thermostating techniques for large many-particle systems, followed by an introduction to the simulation strategies and the protein system considered in this work. Then, in "Results and discussion", we present the simulation results and assess the reliability of the different calculation techniques with regard to data from recent experiments. Finally, we end our paper with a summary and a brief outlook.

Methods

Electrostatics

Simulation of protein–solvent systems generally involves the accurate handling of a huge amount of bonded and non-bonded many-body interactions. A key issue in such simulations is the efficient treatment of the non-bonded long-range electrostatic interactions. There are currently three prevalent methods to treat electrostatic interactions in simulations under periodic boundary conditions [29, 32]: (1) straight truncation of the Coulomb interactions at a convenient cutoff distance [32], (2) smooth truncation of the Coulomb interactions by using a switching or shifting function [28, 33–37] or by including a reaction field (RF) correction [38–40], and (3) application of lattice sum (LS) techniques, like the Ewald summation [41] or related, computationally less expensive methods, such as the PME method [42, 43] or the particle–particle–particle–mesh (P3M) method [44]. Cutoff truncation techniques have the huge advantage of lowering the computational costs and the effect of artificial periodicity in simulations. These properties are important requirements for performing long-time calculations of large protein systems. However, it is well established that straight truncation of the long-range electrostatics represents a severe approximation, leading to numerous artifacts, such as heating, instabilities in the numerical integration procedure as well as inaccuracies in the simulated properties [29]. To alleviate the problem, electrostatic calculation techniques based on switching and shifting functions have been developed, which go to zero smoothly and reduce in this way some of the difficulties caused by abrupt truncation. In many cases, however, they lead to an amplification of other undesirable effects [29]. For example, it has been observed that simulations with atom-based switching functions show artifacts when a too-short switching range is chosen [45]. Instead of that, simulations with a shifted potential provide a too-large root mean square deviation for cutoff criteria less than 14 Å but show reasonable fluctuations with larger cutoffs [28]. However, in a recent study, Yonetani [46] found that in computer simulations of TIP3P water an unphysical layer formation can occur when a long cutoff is used. In the twin-range cutoff (TRC) technique [47], the entire electrostatic potential is shifted, to reduce truncation effects, and the interaction range is divided into two parts. The short-ranged part of the electrostatics within a neighbor-list cutoff is calculated every step and the long-ranged part is only determined with a certain neighbor-list update frequency. In a system with two well-separated length- and time-scales, the TRC technique may be adequate and can significantly accelerate the calculation in comparison to other electrostatic techniques. As a costly alternative to treat long-range electrostatics, LS methods can be used, which rely on the Ewald summation or related techniques [29, 41–43]. Nowadays, the Ewald summation is the most widely employed technique for calculating electrostatic interactions in a periodic or pseudo-periodic system. The basic model relies on a system of point charges, mutually interacting through the Coulomb potential. The Ewald method introduces two amendments to this simple model system, which facilitates its calculation significantly [32]. First of all, each ion is effectively neutralized at long range by the superposition of a spherical Gaussian cloud of opposite charges centered on the ion. The Gaussian cloud acts like an ionic atmosphere, which screens the interactions between neighboring charges and ensures that they become short-ranged. The total screened potential is then calculated

by summing over all the ions in the central cube as well as its periodic images on the real-space lattice. Secondly, a second set of Gaussian charges is superposed, this time possessing the same sign as the original point charges however and again located at the center of the ions. Their function is to cancel the effect of the first set of Gaussian charges and to reduce the overall potential to that resulting from the original point charges. The potential, due to these Gaussians, is obtained by solving Poisson's equation and summing the contributions as a Fourier series in reciprocal space. Finally, the complete Ewald sum requires an additional correction term, known as the self-energy correction, arising from the self-interaction of the canceling distribution with its own site. This term must be subtracted from the total sum. As a result, the Ewald summation technique replaces a potentially infinite only conditionally convergent sum in real space by two finite sums, i.e. a short-ranged part that sums quickly in real space and a long-ranged part that sums quickly in Fourier space, in addition to a constant self-energy correction contribution. The particle mesh-based approaches [27] all attempt to accelerate the solution of Poisson's equation under periodic boundary conditions using the advantages of the fast Fourier transform for calculating discrete Fourier transforms. However, they differ in how they transform the continuous charge density, due to the sum of compensating Gaussians, onto a regular three-dimensional grid and in how they compensate for the loss of accuracy introduced in this process. In the case of the PME technique, the Ewald sum is taken in its original form and the complex exponentials, appearing in the reciprocal sum, are approximated by local polynomial interpolation. Although LS and RF methods rely on more or less reasonable approximations for dealing with the long-range component of the electrostatic interactions, some dependence of the calculated properties on the cutoff distance or system size has also been evidenced for these methods [25, 26, 48–52]. Moreover, it has been stated in several works that the long-range periodicity of the Ewald boundary conditions can artificially stabilize local equilibrium structures of peptides and small proteins by inhibiting conformational fluctuations [27]. For example, Lins and Röthlisberger [24] performed a series of MD simulations to investigate the influence of the long-range electrostatics on the folding of the N-terminal H4-histone tail peptide. In their study, they employed three different long-range electrostatic treatments, i.e., spherical cutoff, RF as well as PME technique, and analyzed their effect on the dynamical behavior of the peptide system. They concluded that, among the three tested methods, the PME technique yields the least conformational variation and tends to a structural stabilization around the initial topology of the peptide.

In another study, Hünenberger and McCammon [26] used an approach based on continuum electrostatics to investigate the nature and magnitude of periodicity-induced artifacts on the dynamics and conformational equilibria of biomolecules. In their work, they considered three model applications, i.e., the unfolding of polyalanine oligopeptides, the separation of the strands of a DNA tetranucleotide, as well as the conformational fluctuations of the small hyper-thermophilic protein Sac7d from *Sulfolobus acidocaldaricus*. From these calculations, they deduced that the artificial periodicity can significantly affect the conformational equilibrium of the biomolecules, in each case stabilizing the most compact conformation. Moreover, they found that periodicity-induced artifacts can be enhanced by different system-specific factors, e.g., a solvent of low dielectric permittivity, a non-negligible solute size compared to the size of the unit cell, or a non-neutral solute. In a further study, Weber et al. [25] investigated the consequences of artificial periodicity on the conformational equilibrium of a polyalanine octapeptide in water. To this end, they performed explicit solvent MD simulations at different system sizes, using the P3M method for handling electrostatic interactions, and compared the results to continuum electrostatics calculations. From their investigation, they concluded that the R-helical conformation of the polyalanine octapeptide is stabilized by artificial periodicity relative to other configurations, sampled during the simulation runs, and that the stabilizing tendency increases with decreasing system sizes. In summary, all these studies demonstrate that the artificial periodicity imposed by the use of the infinite periodic (Ewald) boundary conditions in the treatment of the long-range electrostatics may significantly perturb the dynamics as well as the conformational fluctuations of peptides and small proteins in explicit solvent simulations. However, their influence on the electrostatics of larger protein systems still needs to be assessed.

Thermostating

The influence of thermostating on the structure and dynamics of proteins is well known and has been studied extensively in recent years [31]. However, no ideal thermostating strategy has been developed so far to reproduce protein relaxation under experimental conditions. A standard procedure for controlling the temperature of large biomolecular systems is to make use of the Berendsen thermostat [53]. To maintain the desired temperature, the system is coupled to an external heat bath with fixed temperature T_0 by re-scaling the velocities at each timestep so that the rate of change of the temperature is proportional to the difference in temperature $\mathrm{d}T(t)/\mathrm{d}t = (T_0 - T(t))/\tau$. In this scheme, τ is an empirical heat bath parameter which

determines the strength of the coupling between the physical system and the heat bath. The procedure provides an exponential decay of the kinetic temperature towards the desired temperature. In practice, the parameter τ has to be chosen with care since in the limit $\tau \rightarrow \infty$ the Berendsen thermostat is inactive and the system recovers temperature fluctuations of magnitude of the microcanonical ensemble, while in the case of a too small τ it generates unrealistically small temperature fluctuations [54]. The Berendsen thermostat is widely used to equilibrate biomolecular simulations because of its stability and efficiency in relaxing a system to the target temperature [55]. However, it is well established that the ensemble generated by this approach is not consistent with the canonical phase space distribution [53, 55]. Therefore, once the system has reached equilibrium, it is more appropriate to sample the correct canonical ensemble using the Nosé–Hoover thermostat [56–58]. This method relies on the extended system approach of Nosé [56], which mimics the heat bath by introducing an artificial variable s, associated with a fictive mass $Q>0$, as well as a corresponding velocity ds/dt. The advantage of the Nosé–Hoover thermostat is that it has been proven analytically to generate configurations belonging to the canonical ensemble. Moreover, it can easily be extended to reproduce the exact isothermal–isobaric ensemble [56], generally reflecting the external conditions of standard experimental investigations. However, similarly as in the case of the Berendsen thermostat, the size of the heat bath parameter Q in this procedure affects the rate of exchange of the thermal energy between the physical system and the heat bath by determining the magnitude of the temperature fluctuations. A standard way to solve this difficulty is to couple the solute and solvent degrees of freedom to individual thermostats and optimize their respective Q parameters in such a way to ensure a rapid thermal equilibration of the overall system. However, even if such ideal parameters could be found, a problem still remains when simulating systems composed of large protein domains containing covalently or non-covalently bound prosthetic groups, like the flavoproteins considered in this work. Such systems are inherently heterogeneous, involving many different subsets of degrees of freedom with characteristic relaxation times giving rise to regions of different heat diffusion rates. To ensure ergodicity in the corresponding simulations, it must be guaranteed that all the subsets of degrees of freedom can exchange energy among their various forms within the physical system and with the heat bath. To address this problem, Lingenheil et al. [31] recently introduced a non-invasive thermostating strategy, which relies on the idea that an explicit solvent environment represents an ideal thermostat with regard to the magnitude and time correlation of the temperature fluctuations of the solute molecule. Their approach consists in decoupling the solute from the heat bath, which remains solely thermostated by the surrounding solvent by exchanging kinetic energy with the solvent molecules through particle collisions. From test simulations with peptides, they concluded that this temperature control strategy permits to obtain a homogeneous temperature distribution in equilibrated systems while allowing the solute molecule to sample conformations from the correct statistical ensemble and ensuring a minimal perturbation of its dynamics. Very recently, we have applied the non-invasive thermostating strategy to elucidate the signal transduction pathway of the LOV2-Jα-photosensor from *A. sativa* and could demonstrate that this technique allows to sample protein configurations far from equilibrium and to follow its natural dynamics under solvent-mediated thermostating control [59]. In the following sections, we will compare this technique to the more conventional invasive thermostating strategy and analyze its consequences on the solution structure as well as the conformational fluctuations of the heterogeneous protein domain considered herein.

Our simulation strategy

To ensure isothermal–isobaric conditions in our MD simulations, we adopted the Parrinello–Rahman barostat [58] and the invasive as well as non-invasive thermostating strategy in conjunction with the Nosé–Hoover thermostat. We imposed a heat bath temperature of 300 K by making use of a thermostat coupling constant of $\tau_T = 0.1$ ps and an external pressure of 1 atm by employing a barostat coupling constant of $\tau_P = 0.1$ ps as well as a compressibility of $\beta_T = 4.5 \times 10^{-5}$ bar^{-1}. We integrated the equations of motions, using the leap-frog integrator with a timestep of 1 fs. In every simulation, we equilibrated the solvated protein for 1 ns and then started a production run of 20 ns either by keeping the thermostats coupled to the solute and the solvent (invasive strategy) or by switching to the non-invasive thermostating strategy. In the case of the non-invasive strategy, the protein and FMN chromophore were decoupled from their respective thermostats, while the solvent remained coupled to its thermostat throughout the whole production run. For the treatment of the long-range electrostatics, we used the PME as well as TRC technique. In case of the PME technique, we employed a Coulomb cutoff of 1.4 nm, a PME order of 4 and a neighborlist cutoff of 1.4 nm, determining full electrostatics every timestep on a 54×54×54-Å grid. For the evaluation of the van der Waals (vdW) interactions, we used the shifting function technique with a vdW cutoff of 1.4 nm. In our TRC simulations, we adopted a Coulomb and vdW cutoff of 1.8 nm as well as a neighbor-list cutoff of 1.0 nm with a neighbor-list update frequency of 10.

Program and system

For our simulations, we used the GROMACS molecular dynamics simulation package version 3.3.1 in conjunction with the GROMOS96 43A1 forcefield [60] and applied harmonic bond potentials to describe the bonded interactions of the protein. This widely used forcefield has been tested against NMR spectroscopic data in the case of the hen egg white globular protein lysozyme in water by Soares et al. [61] and has been found to reproduce its solution structure and conformational behavior very well. In a recent work, Todorova et al. [62] performed extensive molecular dynamics simulations on the 51-amino-acid protein insulin and subjected the GROMOS96 43A1 forcefield to a systematic comparison against other popular biomolecular forcefields, including the CHARMM27, AMBER03, OPLS, and GROMOS96 53A6 forcefields. They analyzed in detail the effect of each forcefield on the conformational evolution and structural properties of the protein and compared the results with the available experimental data. They observed that each forcefield favors different structural trends. Moreover, they found that the united-atom forcefield GROMOS96 43A1, together with the CHARMM27 forcefield, delivered the best description of the experimentally observed dynamic behavior of the chain B of insulin. As a starting configuration, we employed the protein crystal structure of the wild-type LOV1 domain of *C. reinhardtii*, which was determined in the X-ray diffraction experiments of Fedorov et al. [12] (PDB-code: 1N9L). The corresponding secondary structure and the local environment of amino acids surrounding the FMN chromophore are visualized in Figs. 1 and 2, respectively. The protein was centered in a cubic box with a box length of 6.09 nm, and the box was filled with 7,005 SPC-216 water molecules. The total charge of the system was neutralized by adding one supplementary sodium ion. The protonation states of the amino acids as well as the one of the phosphate groups at the terminal end of the oxetyl chain of FMN were chosen for the physiologically relevant pH value of 8, which under these conditions means a fully deprotonated phosphate group.

Results and discussion

We start our investigations of the influence of the long-range electrostatics on the conformational heterogeneity of dark-state conformers by performing MD simulations with the PME as well as TRC technique in conjunction with the non-invasive thermostating strategy introduced previously. In Fig. 3, we present results for the time-dependent behavior of characteristic inter-atomic distances of amino acids, either involved in the adduct formation process or forming H-bonds with the FMN chromophore. In Fig. 3a, we show the distance between the adduct-forming reaction centers, i.e., the sulfur atom Cys57-S on the apo-protein and the FMN–C4a atom on the chromophore, as a function of simulation time. We see that the curve, generated with the TRC technique, jumps from a distance of about 4.5 to 7 Å at around 2.5 ns after the start of the production phase, while the curve obtained with the PME technique provides a similar jump after 17 ns. In the next three plots of Fig. 3, we visualize the distances of the H-bond forming acceptor atom FMN-O4 with the donor atoms of the surrounding amino acids Asn89-ND2, Asn99-ND2 as well as Gln120-NE2. In the case of the TRC technique, we observe that the distances between the atoms Asn89-ND2 and FMN-O4, as well as the atoms Gln120-NE2 and FMN-O4, remain stable over the whole simulation time, while the distance between the atoms Asn99-ND2 and FMN-O4, after a sharp increase at around 1 ns, fluctuates about an average value of 8 Å with a large magnitude. By contrast, in the case of the PME

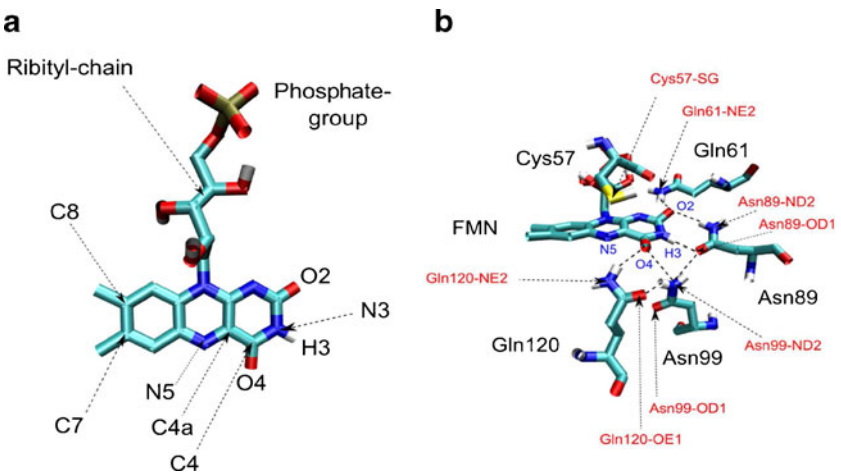

Fig. 2 **a** FMN and **b** crystal conformation of FMN with surrounding amino acids, obtained by Fedorov et al. using X-ray diffraction [12] (MD starting structure)

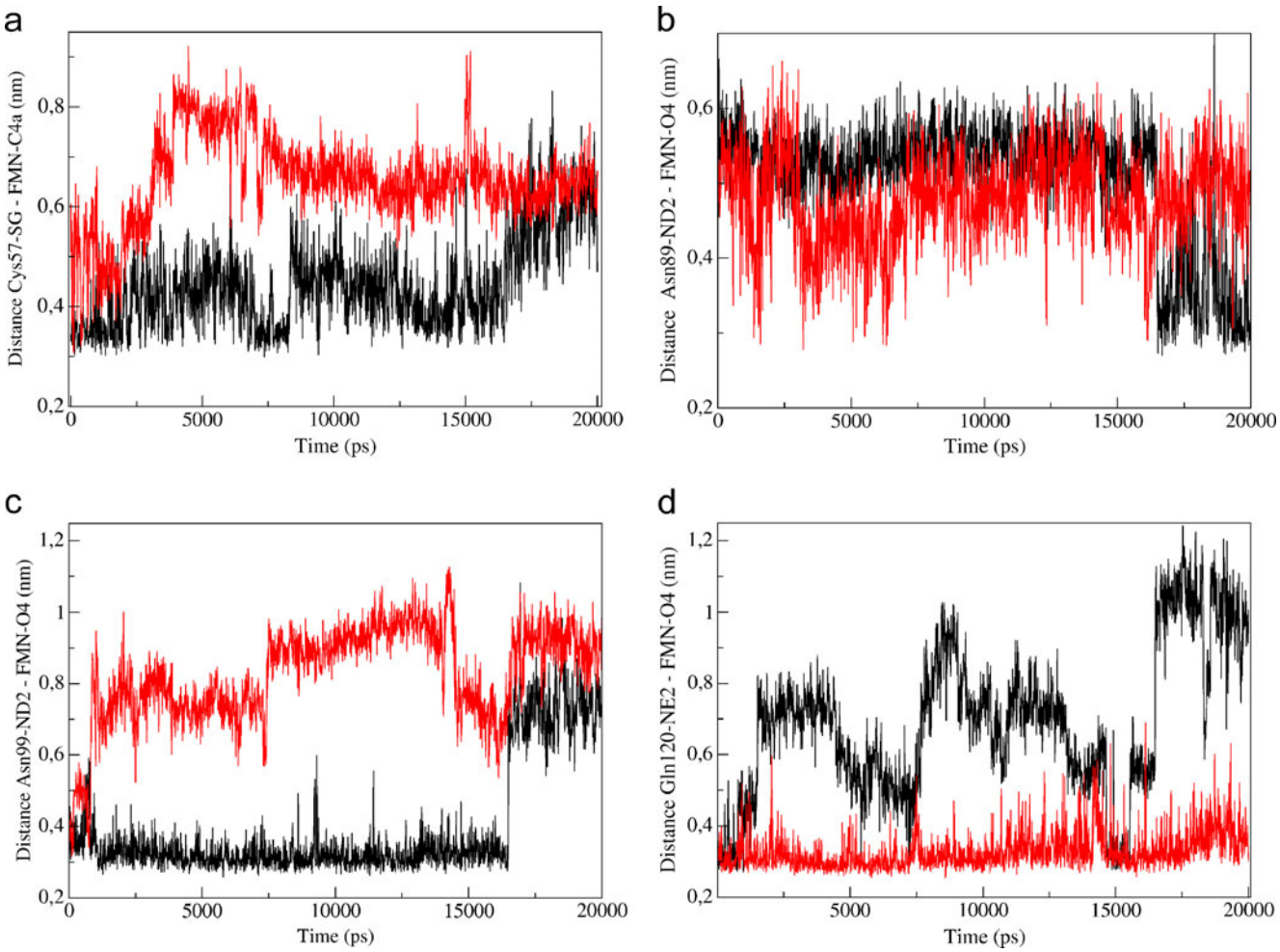

Fig. 3 Distance of characteristic atoms on the FMN chromophore to atoms of the surrounding amino acids calculated with different electrostatic calculation techniques (*black*, non-invasive PME; *red*, non-invasive TRC) in conjunction with the non-invasive thermostating scheme [**a** Cys57-S - FMN–C4a, **b** Asn89-ND2-FMN-O4, **c** Asn99-ND2-FMN–O4, **d** Gln120-NE2 -FMN–O4]

technique, the distances between the atoms Asn89-ND2 and FMN-O4, as well as the atoms Asn99-ND2 and FMN–O4, fluctuate with a moderate magnitude around their average values up to 17 ns, followed by a sharp transition and stabilization around new average values. This sudden structural re-arrangement of the H-bond network concords well with the change in distance between the reaction centers Cys57-S and FMN–C4a at the same simulation time. Moreover, we observe by comparing the results from the TRC and PME technique that after the simulation time of 17 ns nearly the same distances are reached for the reaction centers Cys57-S and FMN–C4a, as well as the H-bond centers Asn99-ND2 and FMN-O4. To analyze these local structural changes on a molecular basis, we visualize in Fig. 4 the representative structures before and after the re-arrangement of amino acids, generated with the TRC and PME technique. If we first compare the two conformations in Fig. 4a, b obtained with the TRC simulations before and after the structural re-arrangement at 2 ns, we notice that the arrangement of the amino acids with respect to FMN remains essentially the same, but the distances of Cys57 and Asn99 with respect to FMN become larger in agreement with the observations made in Fig. 3. By next comparing the conformation obtained with the PME technique before the structural re-arrangement, i.e., Fig. 4c, with the crystal structure of Fedorov et al. in Fig. 2b, we conclude that in the initial part of the production phase the amino acids surrounding the FMN remain stable and fluctuate around the average positions preset by the starting crystal configuration. In particular, we note that in this time range the carbonyl-oxygen atoms O2 and O4 on FMN are twice H-bonded by the hydrogen atoms of the amino acid pairs Gln120 and Asn99 as well as Asn89 and Gln61, respectively. By subsequently comparing the conformations obtained with the PME technique before and after the structural re-arrangement in Fig. 4c, d, we see that the amino acids Gln120, Asn99, Asn89, and Gln61 in the latter case have been displaced with respect to the FMN

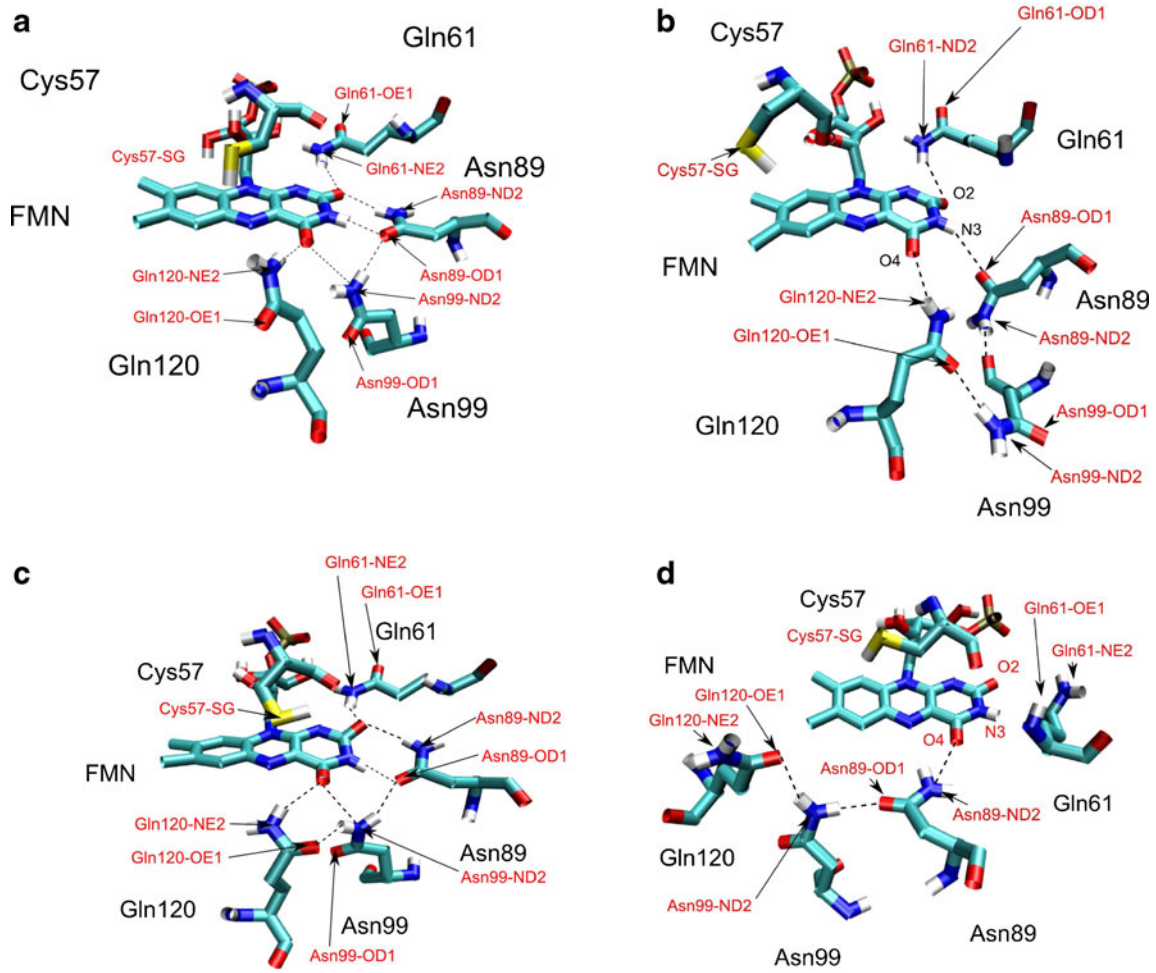

Fig. 4 Representative local configurations of amino acids surrounding the FMN chromophore, obtained with the non-invasive TRC and PME technique [**a** configuration at start of production phase with TRC non-invasive, **b** configuration at 20 ns with non-invasive TRC, **c** configuration at start of production phase with non-invasive PME, **d** configuration at 20 ns with non-invasive PME]

plane, resulting in the formation of a new H-bond network and leaving the orientations of the amino acids with respect to each other unchanged. Moreover, we note that the carbonyl-oxygen atom O4 on FMN, which was originally twice H-bonded with the surrounding amino acid pair Asn99 and Gln120, becomes now singly H-bonded with the amino acid Asn89 in the time range after 17 ns. This observation is sustained by the drop in the distance at 17 ns of the H-bond centers Asn89-ND2 and FMN–O4 in Fig. 3b. Moreover, we further deduce from Fig. 4c, d that the thiol group of the Cys57 residue, which was originally located close to the reactive C4a atom, has in the new configuration re-oriented towards the aromatic benzene ring of the FMN. To analyze this issue in more detail, we present in Fig. 5 the distance between the reactive C8 position on the benzene ring of FMN and the reaction center Cys57-S, calculated with the non-invasive PME technique. We deduce from the figure that, in the time range after 17 ns, the thiol group gets about 4 Å close to the FMN–C8 position, which enables orbital overlap between the new reaction centers and hinders at the same time the process of adduct formation as we will see in the further development. Therefore, the abrupt re-arrangement of the

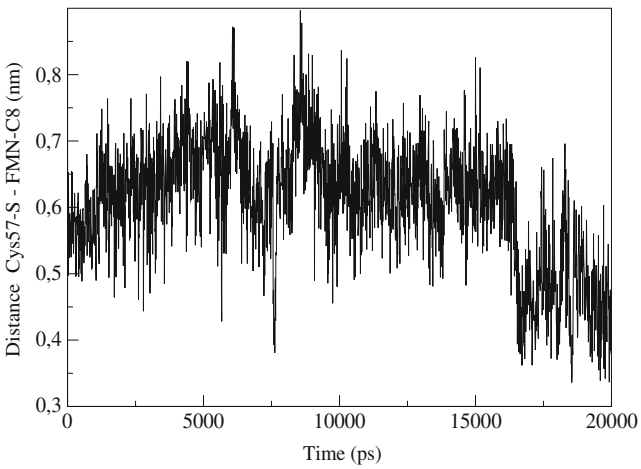

Fig. 5 Distance between the atoms FMN–C8 and Cys57-S, obtained with the non-invasive PME technique

amino acids Cys57, Asn89, Asn99, and Gln120 in vicinity to the FMN indicates the existence of an additional dark-state configuration. This configuration is only temporarily stable and can switch reversibly back to the original configuration. The latter conclusion is supported by our simulation results for the dimers, composed either from LOV1 domains in their dark- or light-state form. In Fig. 1Sa, 1Sb of the "Electronic supplementary material", we present the distances between Asn89-ND2 and FMN–O4 in both monomers of the dark-state (black) and light-state (red) dimers, respectively. From both dark-state curves, we deduce that the distances reversibly jump from about 5.5 to 3.5 Å in both monomers of the dark-state dimer, which agrees well with the behavior of the same quantity in Fig. 3b of the dark-state monomer. In the time ranges, where the distance between Asn89-ND2 and FMN–O4 in the dimer is at 3.5 Å, the carbonyl-oxygen atom O4 on FMN becomes singly H-bonded with the amino acid Asn89, which is characteristic for the second dark-state conformer observed in the monomeric LOV1 domain at 17 ns in Fig. 3b. By contrast, in the time ranges where the distance between Asn89-ND2 and FMN–O4 is at 5.5Å, Asn89-ND2 forms an H-bond with the carbonyl-oxygen atom O2, which is characteristic for the first dark-state conformer. The second conformer can be suppressed upon illumination through adduct formation, as we can deduce from the corresponding results for the light-state dimer in Fig. 1Sa, 1Sb. From these observations, we conclude that both dark-state configurations must be part of an equilibrium distribution of dark-state conformers, which can be influenced through light activation. These findings concord well with the results from the experiments of Kennis et al. [18] in which the molecular mechanism of signal transduction of the phot1 LOV2 domain from *A. sativa* AsLOV2-Jα has been investigated using FTIR spectroscopy. In their study, a structural heterogeneity for AsLOV2-Jα has been reported, involving two different equilibrium populations of C4=O conformers coexisting in the dark. These two conformers were characterized by different C4=O–carbonyl stretching frequencies, which could be attributed either to a singly or twice H-bonded C4=O. Moreover, they have been found to display slightly shifted UV–vis absorption spectra, resulting in a structured absorption band at 475 nm at room temperature and a splitting of this band at low temperatures. Kennis et al. proposed that, in the case of the singly H-bonded conformer, an H-bond is formed between the hydrogen of the amino group of Gln120 and FMN–O4, while in our study we find in contrast that an H-bond is formed between the amino acid Asn89 and FMN–O4. In the following sections, we will analyze in more detail the structural changes involving the amino acid Cys57 because of its role as a reactive residue in the adduct formation process. To this end, we show in Fig. 6 representative structures corresponding to different thiol orientations before and after the structural re-arrangement. By comparing both structures, we recognize that through the structural re-arrangement, the Cys57 thiol group rotates about an angle of 50° with regard to the FMN longitudinal axis and tends towards the C8 position of the FMN. It is worth noting in this context that such configurations have been proposed in various experimental works. In their X-ray diffraction experiments, Fedorov et al. [12] detected two Cys57 rotamers with an occupancy ratio of about 70%:30%, where in the more occupied conformation the thiol group of Cys57 is located about 3.8 Å from FMN–C5a and 4.4 Å from FMN–C4a, while in the less occupied conformation the thiol group is located about 3.5 Å from FMN–C4a. These findings have been confirmed by the FTIR difference spectroscopy experiments of Bednarz et al. [13]. They found that the two conformations are characterized by two different S–H vibrational modes of Cys57, which can be assigned to an H-bond-free state and an H-bonded state. In our simulation study, we find that the FMN–N5-atom stays H-bonded with the reactive Cys57 residue in the time range before the structural re-arrangement, while the H-bond gets disrupted in the time range after the re-arrangement. Kennis et al. [63] suggested in the case of LOV2 that the presence of the thiol group of

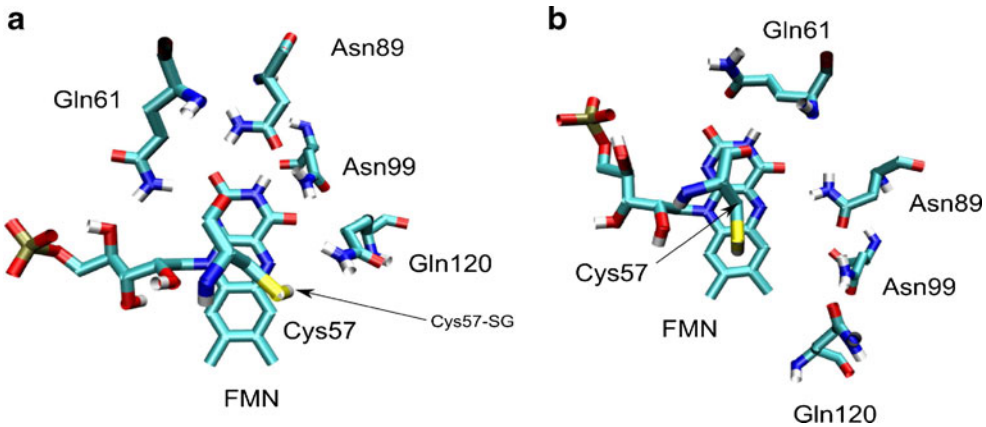

Fig. 6 Representative configurations showing the orientations of the Cys57-thiol group with regard to the FMN ring **a** before and **b** after the structural re-arrangement, obtained with the non-invasive PME technique

the reactive cysteine residue in vicinity of the aromatic ring of FMN shifts the resonance equilibrium away from the oxidized form of FMN to one of its quinoid forms, which is depicted in Fig. 2S of the "Electronic supplementary material". They concluded this by comparing vibrational spectra from fluorescence line narrowing experiments of the wild-type LOV2 species AsLOV2 and Phy3LOV2 with a cysteine-less mutant AsLOV2-C450A [63]. They found that the mutant shows small but significant frequency shifts of the FMN ring vibrations as well as of the C2=O mode with respect to the wild-type species, similar to those found in FMN model systems with an electron-donating group substituted at the C8 position of the FMN. Such substituents are known to induce a quinoid character to the electronic structure of oxidized flavin [64–67], although with smaller absolute frequency shifts than in the case of the non-covalently bound cysteine residue. Kennis et al. concluded that the induction of the quinoid resonance structure by the Cys57 residue may consequently strengthen the H-bond between the amino group of Asn89 and FMN–C2=O and stabilize in this way the H-bond network configuration that enables adduct formation. Moreover, they proposed that it increases the intersystem crossing (ISC) rate by rapid generation of the reactive FMN triplet state, leading to a shortening of the FMN singlet excited-state lifetime. These conclusions are consistent with several experimental studies, which state that the presence of the reactive cysteine at about 4 Å of the FMN [12, 68, 69] is responsible for a shortening of the singlet excited state lifetime and increase of the ISC rate by a factor of 2–3 as compared to FMN in solution [63, 70] or cysteine-less mutants [71, 72]. In this context, it is worth pointing out that in LOV domains an efficient ISC rate is crucial. This relates to the fact that the biologically active adduct state is generated from the first excited triplet state of FMN, which is itself formed through ISC from its first excited singlet state with a high quantum yield of about 60–80% [11, 70, 71, 73–75]. In several experimental studies [12, 70, 71], it has been speculated that the enhanced ISC rate in LOV domains is caused by a heavy-atom effect induced by an interaction between the cysteine sulfur and the flavin isoalloxazine ring. This issue has subsequently been investigated in more detail in a series of theoretical studies. Dittrich et al. [20] performed quantum chemical calculations for the first excited triplet state of the FMN–related model compound lumiflavin at the ROHF/6-31G(2d,2p) level of theory and concluded from analyzing the resulting Mulliken spin populations that a significant fraction of unpaired spin density is localized on the C4a as well as the C8 position of lumiflavin. Salzmann et al. [76, 77] demonstrated that not only the ordering of low-lying potential energy hypersurfaces but also the mechanism of triplet generation in the case of FMN–related compounds significantly depends on the environment. In a recent work, Salzmann et al. [78] explored the ground and low-lying excited states of FMN in the LOV domain of the blue-light photosensor YtvA of *Bacillus subtilis* by means of combined QM/MM methods. They found increased spin–orbit coupling between the initially populated S1 state and the T1 and T2 states in YtvA–LOV compared to free lumiflavin in water. In addition, an external heavy-atom effect was observed when the sulfur atom of the nearby cysteine residue was included in the QM region, which is in line with experimental findings. The electronic interaction between the π_{H-1}-molecular orbital of the isoalloxazine ring and the p_S-lone pair on sulfur was particularly pronounced for the conformation where the thiol group of the reactive cysteine residue C62 tends towards the aromatic ring away from the C4a position of FMN. Similar structural heterogeneities of the reactive cysteine residue have also been found in MD investigations with LOV2 domains [15, 22]. However, no structural re-arrangement of the surrounding amino acids has been detected in these cases. In summary, based on our calculation results and the conclusions from the comparative works presented previously, we retain that the LOV1 domain from *C. reinhardtii* is able to alter its ISC rate from the first excited singlet state to the first excited triplet state by adjusting the orientational distribution of the thiol group of the Cys57 residue towards the C4a and C8 position. The regulation takes place by stabilizing the unpaired spin fractions at the sites FMN–C4a as well as FMN–C8 through electronic interaction between the *p*-lone pair sulfur orbitals of Cys57 with the π-molecular orbitals of the FMN.

To understand the effect of the change of the local H-bond network surrounding the FMN on the overall secondary structure of the LOV1 domain, we study next the overall protein conformations for different local arrangements of amino acids obtained in different time ranges of our non-invasive PME simulations. In the following sections, we first examine the hydrophilic side of the protein domain by visualizing in Fig. 7a, b the protein conformations obtained before and after the structural re-arrangement of amino acids, respectively. From the figures, we observe that a quite large α-helical element, comprising the sequence of amino acids from 32 up to 38 and denoted as Dα in Fig. 1, disappears in the second dark-state conformer after the structural re-arrangement at 17 ns and is converted into an extended unstructured protein chain. This process goes along with the re-orientation of the thiol group of the Cys57 residue towards the FMN–C8 position on the benzene ring of the FMN as well as the re-arrangement of the amino acids Asn89, Asn99, and Gln120 surrounding the FMN. Next, we consider in Fig. 7c, d the corresponding hydrophobic side of the LOV1 domain, essentially characterized by the

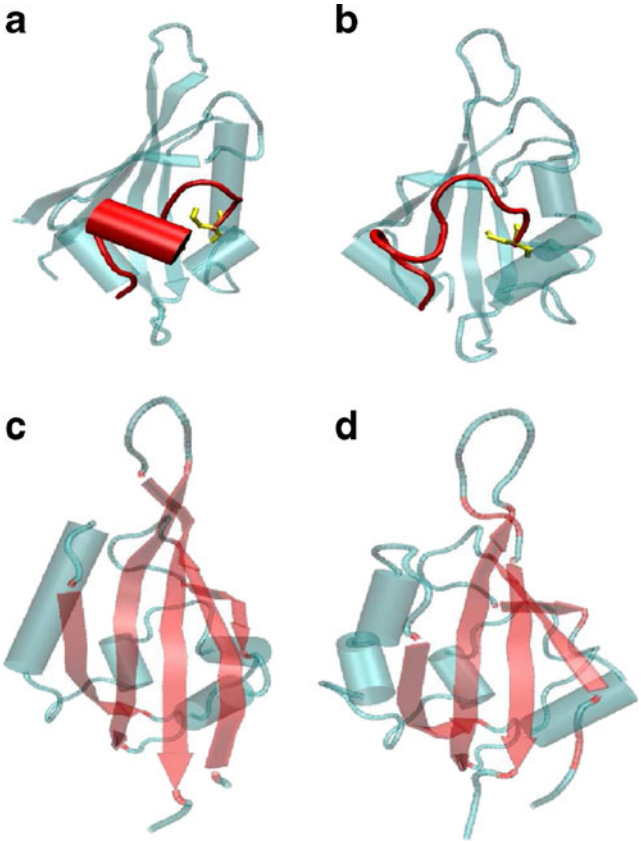

Fig. 7 Protein structure of the wild-type LOV1 domain at different times using the non-invasive PME simulation technique [**a** hydrophilic side at start of production phase, **b** hydrophilic side at 20 ns, **c** hydrophobic side at start of production phase, **d** hydrophobic side at 20 ns]

alignment of the β-strands. We observe that, due to the loss of structure of the Dα-helix, the tightening of the β-sheet is reduced and the flexibility of the β-strands is augmented in the second dark-state conformer, which increases the ability of the LOV1 domain for dimerization through this site with other LOV domains or the kinase. As demonstrated in Fig. 1Sa, 1Sb on the example of dimers formed from the dark state LOV1 domains, this conformer is only temporarily stable both in its monomeric and dimeric form and can reversibly switch back to the original configuration. This indicates that the LOV1 domain is able to modulate its dimerization tendency in the dark through this α-helical element by increasing its capacity to adjust onto the hydrophobic surface of its respective partner domain. These conclusions are confirmed through our simulation results for various α-helical elements of the LOV1 dimer presented in Fig. 3S, where we considered both monomers either in their dark- or light-state form. In these graphs, we show the center-of-mass distances as a function of simulation time between α-helices located on different LOV1 domains. From Fig. 3Sa, 3Sb, we deduce that after an initial adjustment phase the Cα- and Fα-helices, flanking the β-sheets in the monomers, come more close to each other by about 3 Å at 10 ns in the dark-state dimer compared to the light-state dimer. This enhances the affinity of the LOV1 domains for docking via their accommodated hydrophobic surfaces on the β-sheets. This docking process goes along with an increase of the distance of the Dα-helices by about 5Å in Fig. 3Sc, which together with the increased distance between the Eα-helices in Fig. 3Sd results in an overall enlargement of the volume of the dark-state dimer with respect to the light-state dimer. The previous analysis is confirmed in Fig. 4S where we show the dimeric structures of the LOV1 domains in their dark- and light-state form after a simulation time of 20 ns. Moreover, from the fact that the structural re-arrangement of amino acids surrounding the FMN chromophore can be suppressed through light activation, we infer that the distribution of dark-state conformers might play a role in controlling the docking affinity. In this context, it is worth pointing out that our conclusions concord well with several recent experimental works [7, 79], where it has been suggested that the alignment of the β-sheets is responsible for controlling the dimerization process of the LOV1 domains and might regulate, in this way, the signal intensity of the phototropin under different light conditions. Since the equilibrium of dark-state conformers of the LOV1 domain can be influenced by light activation or a change of external conditions, e.g., a change in temperature, shifting their population distribution might permit the LOV1 domain from *C. reinhardtii* to act as a modulator, which may allow a fine-tuning of its signal response to a change in its environment.

In order to assess the influence of different electrostatics on the conformational fluctuations and the effect of the structural re-arrangement of amino acids near the chromophore on the secondary structure of the LOV1 domain, we consider next in Fig. 8 the results from the secondary structure analysis of the MD trajectories, obtained with the non-invasive TRC and PME simulation technique. By comparing the parts of the sequence forming β-strands, we observe that, although the overall secondary structure is preserved with both simulation strategies, the TRC technique provides larger fluctuations in comparison to the PME technique, leading to a reduction in the size of the β-strands. A similar reduction in size can be observed for the α-helical elements known as the Fα- and Cα helices, comprised between the residue numbers 50 and 64 as well as 22 and 30, respectively. Another clear difference between both techniques appears in the secondary structure in the vicinity of the chromophore. While the TRC technique favors the formation of the Eα-helix after 12 ns within the range of residue numbers 41 to 46, the PME technique favors the disappearance of the Dα-helix after

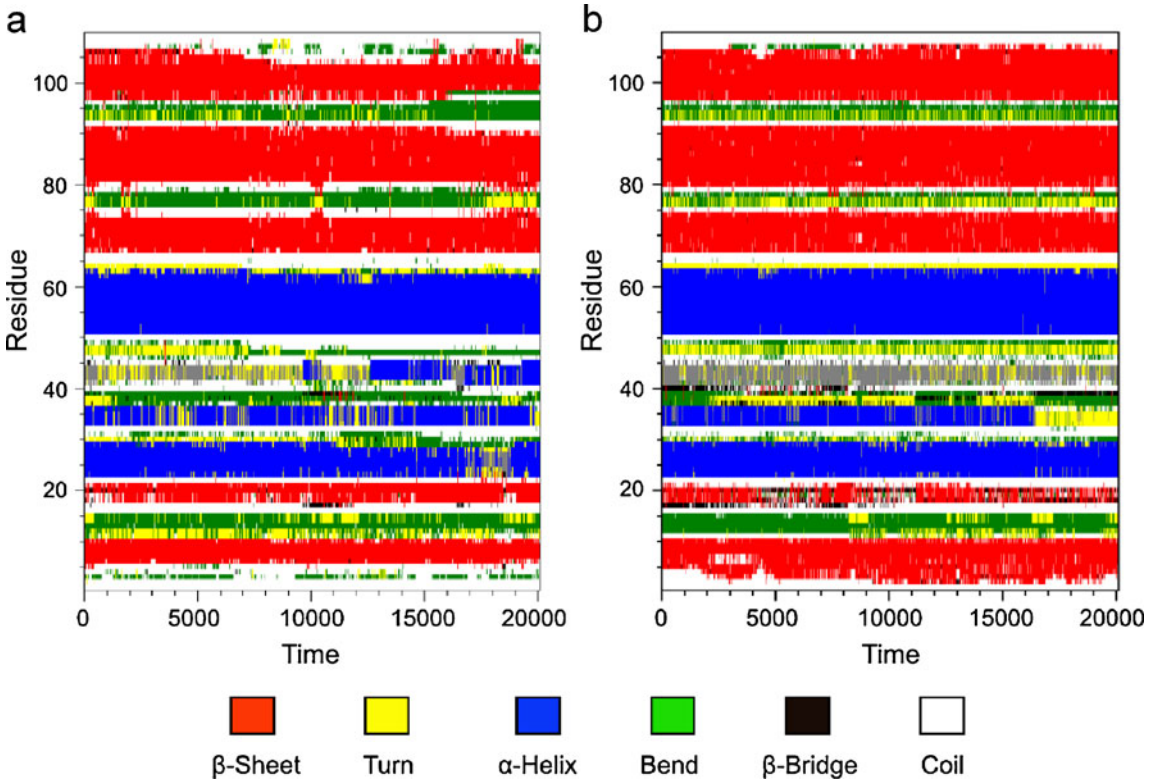

Fig. 8 Secondary structure analysis of non-invasive simulation trajectories of the wild-type LOV1 domain, using different electrostatic calculation techniques [**a** TRC technique, **b** PME technique]

17 ns, which directly correlates with the structural re-arrangement of the amino acids around the chromophore depicted in Fig. 4c, d. The direct response of the secondary structure to local re-arrangements of the H-bond network in conjunction with the preservation of the remaining secondary structure of the protein domain indicates that the non-invasive PME technique has generated an additional dark-state conformer of the wild-type LOV1 domain in the time range after 17 ns. By contrast, the formation of the Eα-helix in the case of the TRC technique cannot be correlated with a local re-arrangement of the amino acids near the chromophore, as can be deduced from Fig. 4a, b. The generation of this new helical element appears to take place at the expense of a weakening of the binding interaction with the chromophore and a strengthening of low-mode fluctuations, leading to a partial destabilization of the remaining secondary structure. This tendency can further be confirmed by regarding the kinetic temperature across the LOV1 domain–solvent system, which is an important indicator for assessing the stability of the simulation and efficiency of the thermostating scheme. To this end, we show in Fig. 9 the time evolution of the kinetic temperatures from the FMN chromophore (black), the apo-protein (red) as well as the solvent (green), obtained by using the non-invasive thermostating strategy in conjunction with the TRC as well as PME technique. In the case of the TRC technique, we observe a slow drift of the temperature of the FMN chromophore and protein, which relates to the fact that the system is unstable due to the electrostatic calculation technique. This behavior is also reflected by considering the average kinetic temperatures produced by the TRC technique: $< T_{\mathrm{TRC}}^{\mathrm{FMN}} >= 308.262 \pm 42.5179\,\mathrm{K}, < T_{\mathrm{TRC}}^{\mathrm{protein}} >= 307.428 \pm 8.66738\,\mathrm{K}$, and $< T_{\mathrm{TRC}}^{\mathrm{solv}} >= 300 \pm 2.12618\,\mathrm{K}$. By contrast, in the case of the PME technique, the kinetic temperatures are perfectly stable over the entire simulation run and fluctuate around the externally imposed temperature of 300 K, differing solely in the magnitude of the fluctuations. The PME technique provided the following average temperatures: $< T_{\mathrm{PME}}^{\mathrm{FMN}} >= 300.871 \pm 41.2056\,\mathrm{K}, < T_{\mathrm{PME}}^{\mathrm{protein}} >= 301.082 \pm 7.52788\,\mathrm{K}$, and $< T_{\mathrm{PME}}^{\mathrm{solv}} >= 300 \pm 2.12519\,\mathrm{K}$. The larger fluctuations of the FMN chromophore can be easily explained by the fact that in the dark state of the LOV1 domain the chromophore is unbounded in the binding pocket, which results in stronger fluctuations. In conclusion, these observations provide further evidence that the non-invasive PME technique is more reliable compared to the TRC technique in reproducing the structures and conformational behavior of the LOV1 domain–solvent system.

As we discussed in "Thermostating", the protein dynamics, besides the electrostatics, can also be tremendously affected by the thermostating procedure. To investigate this aspect, we performed simulations with the PME

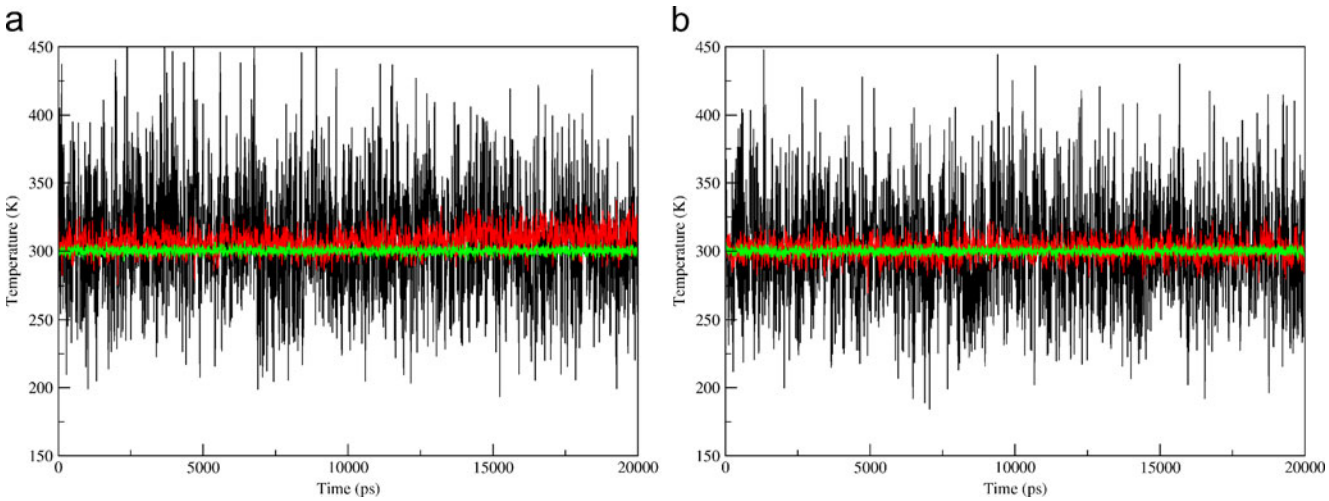

Fig. 9 Kinetic temperatures from the FMN chromophore (*black*), the apo-protein (*red*) as well as the solvent (*green*) of the wild-type LOV1 domain–solvent system, obtained by using the non-invasive thermostating strategy in conjunction with different electrostatic calculation techniques [**a** TRC technique, **b** PME technique]

technique using the invasive and non-invasive thermostating strategy introduced in the same section. The effects on the dynamics are shown in Fig. 10, where we plot the distances of characteristic atoms on the FMN chromophore to atoms of the surrounding amino acids. From the figures, we deduce that both thermostating strategies provide a different dynamical behavior of the amino acids near to the chromophore. The invasive strategy favors equilibrium fluctuations around the starting crystal configuration by enforcing the same temperature in each part of the system at any time of the simulation. This causes that configurations far from this local equilibrium configuration are suppressed and the system cannot drift towards a new equilibrium configuration. The non-invasive strategy, by contrast, avoids this problem by only thermostating the solvent, which permits the system also to sample configurations far from equilibrium. This is reflected by the sudden local rearrangement of the amino acids at 17 ns and the emergence of a new local equilibrium configuration. By considering that both configurations are in agreement with the experimental observations discussed previously, we conclude that the non-invasive thermostating strategy provides a better thermostating strategy for simulating the protein dynamics and sampling the distribution of dark-state conformers realistically. The importance of the distribution of dark-state conformers for the functionality of the LOV1 domain still needs to be assessed through theoretical as well as experimental means. However, it is plausible that, through a shift in the population distribution of interconverting states, the LOV1 domain is able to adapt to a change of the external conditions, e.g., a temperature change and/or the solvation environment. This might permit the LOV1 domain to act as a modulating sensor with adjustable dark-state activity.

Conclusions

In summary, in the present study, we investigated the influence of the calculation procedure on the dark-state conformers of the wild-type LOV1 domain from the green algae *C. reinhardtii* in its monomeric and dimeric form. In particular, we considered the effect of different long-range electrostatic calculation techniques and thermostating strategies on their solution structures and conformational fluctuations. To this end, we first compared MD simulation results generated with the particle-mesh Ewald and the computationally less expensive twin-range-cutoff technique. The former technique has been suspected in previous works to suppress the conformational fluctuations of peptides and small proteins because of artificial periodicity, while the second technique has been found to lead to an unrealistic destabilization of local configurations. In the particle-mesh Ewald case, we find two local configurations of the amino acids surrounding the FMN chromophore, which can reversibly be inter-converted into each other. In the crystal-like dark-state conformer, the carbonyl-oxygen atom O4 on FMN is twice H-bonded by the surrounding amino acid pair Asn99 and Gln120. In the second dark-state conformer, the carbonyl-oxygen atom O4 on FMN becomes singly H-bonded with the amino acid Asn89, in agreement with experimental observations. Moreover, the thiol group of the reactive Cys57 residue, which in the crystal-like conformer is located close to the reactive center

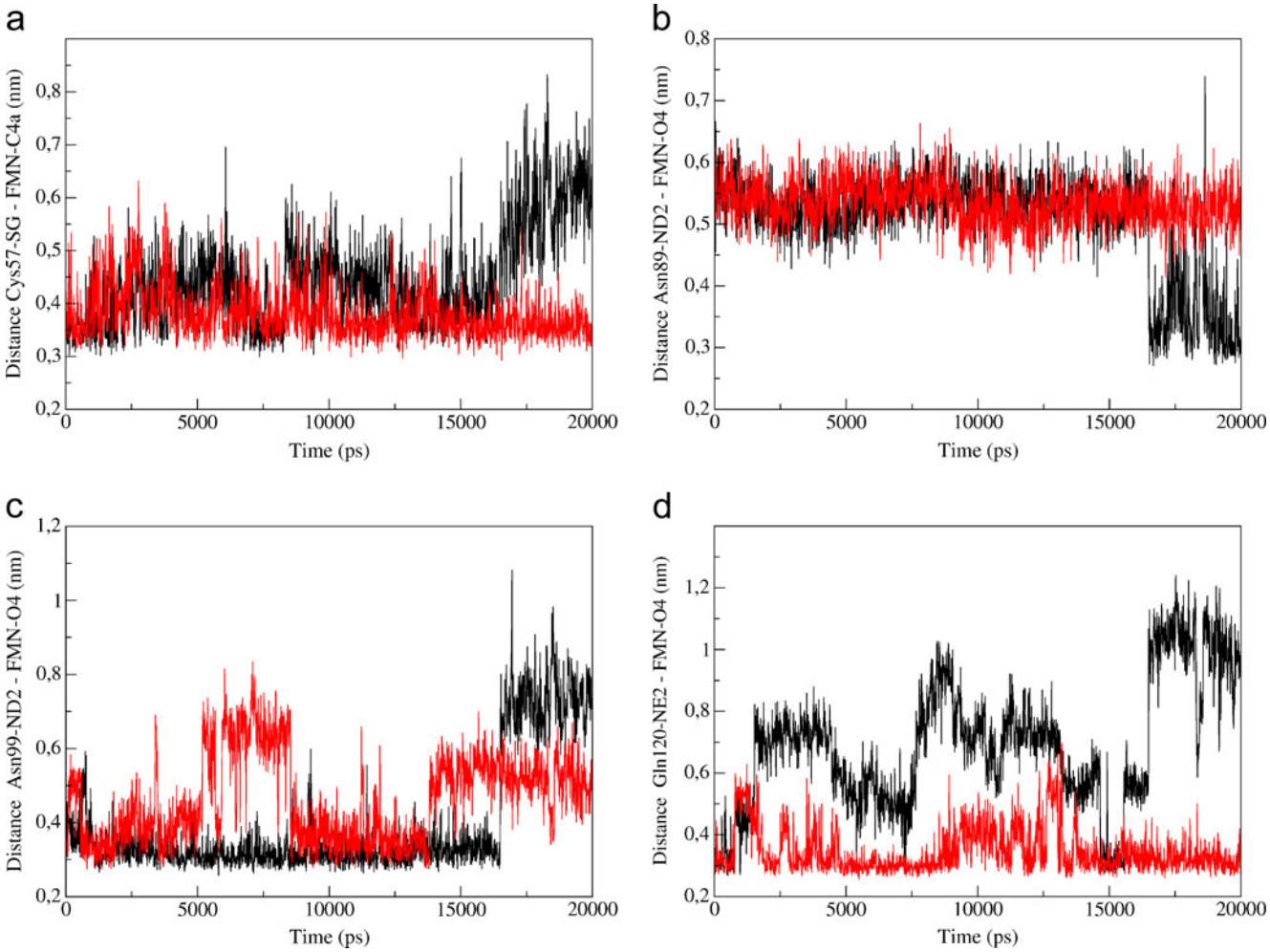

Fig. 10 Distance of characteristic atoms on the FMN chromophore to atoms of the surrounding amino acids, calculated with the PME technique using the non-invasive (*black*) and invasive (*red*) thermostating strategy [**a** Cys57-S-FMN–C4a, **b** Asn89-ND2-FMN–O4, **c** Asn99-ND2-FMN–O4, **d** Gln120-NE2-FMN–O4]

FMN–C4a, points in the second dark-state conformer away from this site and in the direction to the benzene ring of the FMN. Through electronic interaction with the C8 position on this ring, the thiol group can cause a stabilization of the quinoid resonance structure of the FMN and lead to an enhancement of the ISC rate, which promotes the population of the reactive FMN triplet state from which the biologically active adduct state of the protein is generated. Our calculations and the comparative experimental results indicate that the LOV1 domain from *C. reinhardtii* is able to alter the ISC rate and rate of adduct formation by adjusting the population distribution of dark-state conformers. To understand the effect of the local arrangement of amino acids around the chromophore on the overall solution structure of the LOV1 domain, we also compared the protein secondary structures of the two dark conformers. In the second dark-state conformer, we observed the disappearance of an α-helical element, denoted as the Dα-helix, in conjunction with an augmentation of the flexibility of the β-strands, which might increase the capacity of the LOV1 domain to adjust on the hydrophobic surfaces of other LOV domains or the kinase. Therefore, shifting the population distribution towards one or the other conformer via a change of external conditions, e.g., a temperature change, might permit the green algae *C. reinhardtii* to regulate the affinity for dimerization of the LOV1 domains in the dark and provide a mechanism for modulating the response under low light conditions. In the case of the twin-range-cutoff technique, a weakening of the H-bond interactions between the chromophore and the apoprotein as well as a strengthening of low-mode fluctuations is observed, leading to a partial destabilization of the protein secondary structure. Overall, we can say that the twin-range-cutoff technique leads to larger conformational fluctuations resulting in a destabilization of the secondary structure of the protein domain, whereas the PME technique leads to conformational fluctuations in consistency with experimental observations.

Another major goal of this work was to study the effect of the thermostating strategy on the local arrangement of amino acids around the FMN and the conformational fluctuations of the dark-state conformers. To analyze this aspect, we investigated the usefulness of the non-invasive thermostating technique, where the protein solute is only indirectly coupled to the thermostat via the surrounding solvent. We compared this strategy to the standard invasive thermostating strategy where individual thermostats are coupled to both the solute and the surrounding solvent. From our investigation, we deduce that both thermostating strategies provide a different dynamical behavior of the amino acids near to the chromophore. The invasive strategy favors equilibrium fluctuations around the starting crystal structure by enforcing the same temperature in each part of the system at any time of the simulation. This causes that configurations far from this local equilibrium configuration are suppressed and the system cannot drift towards a new local equilibrium. The non-invasive strategy, by contrast, avoids this problem by only thermostating the solvent, which enables the protein to sample configurations far from equilibrium. This permits the sudden local re-arrangement of the amino acids to take place, leading to the emergence of a new local equilibrium configuration. Since the resulting solution structure is in agreement with experimental observations, we conclude that the non-invasive thermostating strategy provides a better thermostating strategy for simulating the protein dynamics and sampling the distribution of dark-state conformers realistically.

Finally, our investigation indicates that, through a shift in the population distribution of dark-state conformers, the LOV1 domain is able to adapt its reactivity to a change of external conditions and act in this way as a modulating sensor. However, the role of the different dark-state conformers for the functionality of the LOV1 domain still needs to be assessed in their natural environment. This requires the development of novel, reliable, cost-effective computational methods to treat multiple length scales [30] and long-range interactions [80] effectively.

References

1. Hegemann P (2008) Algal sensory photoreceptors. Annu Rev Plant Biol 59:167–189
2. Christie JM (2007) Phototropin blue-light receptors. Annu Rev Plant Biol 58:21–45
3. Briggs WR (2007) The LOV domain: a chromophore module servicing multiple photoreceptors. J Biomed Sci 14:499–504
4. Kottke T, Hegemann P, Dick B, Heberle J (2006) The photochemistry of the light-, oxygen-, and voltage-sensitive domains in the algal blue light receptor phot. Biopolymers 82:373–378
5. Jones MA, Feeney KA, Kelly SM, Christie JM (2007) Mutational analysis of phototropin1 provides insights into the mechanism underlying LOV2 signal transmission. J Biol Chem 282:6405–6414
6. Salomon M, Lempert U, Rüdiger W (2004) Dimerization of the plant photoreceptor phototropin is probably mediated by the LOV1 domain. FEBS Lett 572:8–10
7. Kutta RJ, Hofinger ESA, Preuss H, Bernhardt G, Dick B (2008) Blue-light induced interaction of LOV domains from *Chlamydomonas reinhardtii*. ChemBioChem 9:1931–1938
8. Christie JM, Swartz TE, Bogomolni RA, Briggs WR (2002) Phototropin LOV domains exhibit distinct roles in regulating photoreceptor function. Plant J 32:205–219
9. Kagawa T, Kasahara M, Abe T, Yoshida S, Wada M (2004) Function analysis of phototropin2 using fern mutants deficient in blue light-induced chloroplast avoidance movement. Plant Cell Physiol 45:416–426
10. Sullivan S, Thomson CE, Lamont DJ, Jones MA, Christie JM (2008) In vivo phosphorylation site mapping and functional characterization of *Arabidopsis* phototropin1. Mol Plant 1:178–194
11. Kottke T, Heberle J, Hehn D, Dick B, Hegemann P (2003) Phot-LOV1: photocycle of a blue-light receptor domain from the green alga *Chlamydomonas reinhardtii*. Biophys J 84:1192–1201
12. Fedorov R, Schlichting I, Hartmann E, Domratcheva T, Fuhrmann M, Hegemann P (2003) Crystal structures and molecular mechanism of a light-induced signaling switch: the phot-LOV1 domain from *Chlamydomonas reinhardtii*. Biophys J 84:2474–2482
13. Bednarz T, Losi A, Gärtner W, Hegemann P, Heberle J (2004) Functional variations among LOV domains as revealed by FT-IR difference spectroscopy. Photochem Photobiol Sci 3:575–579
14. Schleicher E, Kowalczyk RM, Kay CWM, Hegemann P, Bacher A, Fischer M, Bittl R, Richter G, Weber S (2004) On the reaction mechanism of adduct formation in LOV domains of the plant blue-light receptor phototropin. J Am Chem Soc 126:11067–11076
15. Sato Y, Nabeno M, Iwata T, Tokutomi S, Sakurai M, Kandori H (2007) Heterogeneous environment of the SH group of Cys966 near the flavin chromophore in the LOV2 domain of *Adiantum neochrome1*. Biochemistry 46:10258–10265
16. Iwata T, Nozaki D, Tokutomi S, Kandori H (2005) Comparative investigation of the LOV1 and LOV2 domains in *Adiantum phytochrome3*. Biochemistry 44:7427–7434
17. Iwata T, Nozaki D, Tokutomi S, Kagawa T, Wada M, Kandori H (2003) Light-induced structural changes in the LOV2 domain of *Adiantum phytochrome3* studied by low temperature FTIR and UV–visible spectroscopy. Biochemistry 42:8183–8191
18. Alexandre MTA, van Grondelle R, Hellingwerf KJ, Kennis JTM (2009) Conformational heterogeneity and propagation of structural changes in the LOV2/Jα domain from *Avena sativa* phototropin1 as recorded by temperature-dependent FTIR spectroscopy. Biophys J 97:238–247
19. Neiss C, Saalfrank P (2003) Ab initio quantum chemical investigation of the first steps of the photocycle of phototropin: a model study. Photochem Photobiol 77:101–109
20. Dittrich M, Freddolino PL, Schulten K (2005) When light falls in LOV: a quantum mechanical/molecular mechanical study of photoexcitation in phot-LOV1 of *Chlamydomonas reinhardtii*. J Phys Chem B 109:13006–13013
21. Freddolino PL, Dittrich M, Schulten K (2006) Dynamic switching mechanisms in LOV1 and LOV2 domains of plant phototropins. Biophys J 91:3630–3639
22. Neiss C, Saalfrank P (2004) Molecular dynamics simulation of the LOV2 domain from *Adiantum capillus-veneris*. J Chem Inf Comput Sci 44:1788–1793
23. Arai S, Togashi M, Shiozawa M, Inoue Y, Sakurai M (2005) Molecular dynamics simulation of the M intermediate of photoactive yellow protein in the crystalline state. Chem Phys Lett 414:230–233

24. Lins RD, Röthlisberger U (2006) Influence of long-range electrostatic treatments on the folding of the N-terminal H4 histone tail peptide. J Chem Theory Comput 2:246–250
25. Weber W, Hünenberger PH, McCammon JA (2000) Molecular dynamics simulations of a polyalanine octapeptide under Ewald boundary conditions: influence of artificial periodicity on peptide conformation. J Phys Chem B 104:3668–3675
26. Hünenberger PH, McCammon JA (1999) Effect of artificial periodicity in simulations of biomolecules under Ewald boundary conditions: a continuum electrostatics study. Biophys Chem 78:69–88
27. Sagui C, Darden TA (1999) Molecular dynamics simulations of biomolecules: long-range electrostatic effects. Annu Rev Biophys Biomol Struct 28:155–179
28. Loncharich RJ, Brooks BR (1989) The effects of truncating long-range forces on protein dynamics. Proteins Struct Funct Genet 6:32–45
29. Bergdorf M, Peter C, Hünenberger PH (2003) Influence of cut-off truncation and artificial periodicity of electrostatic interactions in molecular simulations of solvated ions: a continuum electrostatics study. J Chem Phys 119:9129–9144, and references therein
30. Baeurle SA (2009) Multiscale modeling of polymer materials using field-theoretic methodologies: a survey about recent developments. J Math Chem 46:363–426
31. Lingenheil M, Denschlag R, Reichold R, Tavan P (2008) The "hot-solvent/cold-solute" problem revisited. J Chem Theory Comput 4:1293–1306
32. Allen MP, Tildesley DJ (1987) Computer simulation of liquids. Oxford University Press, Oxford
33. Brooks BR, Bruccoleri RE, Olafson BD, States DJ, Swaminathan S, Karplus M (1983) CHARMM: a program for macromolecular energy, minimization, and dynamics calculations. J Comput Chem 4:187–217
34. Brooks CL III, Pettitt BM, Karplus M (1985) Structural and energetic effects of truncating long ranged interactions in ionic and polar fluids. J Chem Phys 83:5897–5908
35. Kim KS (1989) On effective methods to treat solvent effects in macromolecular mechanics and simulations. Chem Phys Lett 156:261–268
36. Steinbach PJ, Brooks BR (1994) New spherical-cutoff methods for long-range forces in macromolecular simulation. J Comput Chem 15:667–683
37. Norberg J, Nilsson L (2000) On the truncation of long-range electrostatic interactions in DNA. Biophys J 79:1537–1553
38. Barker JA, Watts RO (1973) Monte Carlo studies of the dielectric properties of waterlike models. Mol Phys 26:789–792
39. Tironi IG, Sperb R, Smith PE, van Gunsteren WF (1995) A generalized reaction field method for molecular dynamics simulations. J Chem Phys 102:5451–5459
40. Hünenberger PH, van Gunsteren WF (1998) Alternative schemes for the inclusion of a reaction-field correction into molecular dynamics simulations: influence on the simulated energetic, structural, and dielectric properties of liquid water. J Chem Phys 108:6117–6134
41. Ewald PP (1921) Die Berechnung optischer und elektrostatischer Gitterpotentiale. Ann Phys (Leipzig) 64:253–287
42. Darden T, York D, Pedersen L (1993) Particle mesh Ewald: an Nlog(N) method for Ewald sums in large systems. J Chem Phys 98:10089–10092
43. Essmann U, Perera L, Berkowitz ML, Darden T, Lee H, Pedersen LG (1995) A smooth particle mesh Ewald method. J Chem Phys 103:8577–8593
44. Hockney RW, Eastwood JW (1988) Computer simulation using particles. Inst of Physics, Bristol
45. van der Spoel D, van Maaren PJ (2006) The origin of layer structure artifacts in simulations of liquid water. J Chem Theory Comput 2:1–11
46. Yonetani Y (2005) A severe artifact in simulation of liquid water using a long cut-off length: appearance of a strange layer structure. Chem Phys Lett 406:49–53
47. van Gunsteren WF, Berendsen HJC (1990) Computer simulation of molecular dynamics: methodology, applications, and perspectives in chemistry. Angew Chem Int Ed Engl 29:992–1023
48. Hummer G, Pratt LR, Garcia AE (1996) Free energy of ionic hydration. J Phys Chem 100:1206–1215
49. Hummer G, Pratt LR, Garcia AE (1998) Molecular theories and simulation of ions and polar molecules in water. J Phys Chem A 102:7885–7895
50. Hünenberger PH, McCammon JA (1999) Ewald artifacts in computer simulations of ionic solvation and ion–ion interaction: a continuum electrostatics study. J Chem Phys 110:1856–1872
51. Baker NA, Hünenberger PH, McCammon JA (1999) J Chem Phys 110:10679–10692
52. Baker NA, Hünenberger PH, McCammon JA (2000) Erratum: "Polarization around an ion in a dielectric continuum with truncated electrostatic interactions" [J. Chem. Phys. 110, 10679 (1999)]. J Chem Phys 113:2510–2511
53. Berendsen HJC, Postma JPM, van Gunsteren WF, DiNola A, Haak JR (1984) Molecular dynamics with coupling to an external bath. J Chem Phys 81:3684–3690
54. Mor A, Ziv G, Levy Y (2008) Simulations of proteins with inhomogeneous degrees of freedom: the effect of thermostats. J Comput Chem 29:1992–1998
55. Rosta E, Buchete N-V, Hummer G (2009) Thermostat artifacts in replica exchange molecular dynamics simulations. J Chem Theory Comput 5:1393–1399
56. Nosé S (1984) A unified formulation of the constant temperature molecular dynamics methods. J Chem Phys 81:511–519
57. Hoover WG (1985) Canonical dynamics: equilibrium phase-space distributions. Phys Rev A 31:1695–1697
58. Frenkel D, Smit B (2003) Understanding molecular simulation: from algorithms to applications. Academic, San Diego
59. Peter E, Dick B, Baeurle SA (2010) Mechanism of signal transduction of the LOV2-Jα-photosensor from *Avena sativa*. Nat Commun 1:122
60. Lindahl E, Hess B, van der Spoel D (2001) GROMACS 3.0: a package for molecular simulation and trajectory analysis. J Mol Model 7:306–317
61. Soares T, Daura X, Oostenbrink C, Smith L, van Gunsteren WF (2004) Validation of the GROMOS force-field parameter set 45A3 against nuclear magnetic resonance data of hen egg lysozyme. J Biomol NMR 30:407–422
62. Todorova N, Legge FS, Treutlein H, Yarovsky I (2008) Systematic comparison of empirical forcefields for molecular dynamic simulation of insulin. J Phys Chem B 112:11137–11146
63. Alexandre MTA, van Grondelle R, Hellingwerf KJ, Robert B, Kennis JTM (2008) Perturbation of the ground-state electronic structure of FMN by the conserved cysteine in phototropin LOV2 domains. Phys Chem Chem Phys 10:6693–6702
64. Nishina Y, Kitagawa T, Shiga K, Horiike K, Matsumura Y, Watari H, Yamano T (1978) Resonance Raman spectra of riboflavin and its derivatives in the bound state with egg riboflavin binding proteins. J Biochem 84:925–932
65. Nishina Y, Shiga K, Horiike K, Tojo H, Kasai S, Yanase K, Matsui K, Watari H, Yamano T (1980) Vibrational modes of flavin bound to riboflavin binding protein from egg white: resonance Raman spectra of lumiflavin and 8-substituted riboflavin. J Biochem 88:403–409
66. Dutta PK, Spencer R, Walsh C, Spiro TG (1980) Resonance Raman and coherent anti-stokes Raman scattering spectra of flavin derivatives. Vibrational assignments and the zwitterionic structure of 8-methylamino-riboflavin. Biochim Biophys Acta 623:77–83

67. Schopfer LM, Morris MD (1980) Resonance Raman spectra of flavin derivatives containing chemical modifications in positions 7 and 8 of the isoalloxazine ring. Biochemistry 19:4932–4935
68. Crosson S, Moffat K (2001) Structure of a flavin-binding plant photoreceptor domain: insights into light-mediated signal transduction. Proc Natl Acad Sci USA 98:2995–3000
69. Halavaty AS, Moffat K (2007) N- and C-terminal flanking regions modulate light-induced signal transduction in the LOV2 domain of the blue light sensor phototropin1 from *Avena sativa*. Biochemistry 46:14001–14009
70. Kennis JTM, Crosson S, Gauden M, van Stokkum IHM, Moffat K, van Grondelle R (2003) Primary reactions of the LOV2 domain of phototropin, a plant blue-light photoreceptor. Biochemistry 42:3385–3392
71. Holzer W, Penzkofer A, Fuhrmann M, Hegemann P (2002) Absorption and emission spectroscopic characterisation of the LOV2-His domain of phot from *Chlamydomonas reinhardtii*. Photochem Photobiol 75:479–487
72. Schüttrigkeit TA, Kompa CK, Salomon M, Rudiger W, Michel-Beyerle ME (2003) Primary photophysics of the FMN binding LOV2 domain of the plant blue light receptor phototropin of *Avena sativa*. Chem Phys 294:501–508
73. Swartz TE, Corchnoy SB, Christie JM, Lewis JW, Szundi I, Briggs WR, Bogomolni RA (2001) The photocycle of a flavin-binding domain of the blue-light photoreceptor phototropin. J Biol Chem 276:36493–36500
74. Losi A, Polverini E, Quest B, Gärtner W (2002) First evidence for phototropin-related blue-light receptors in prokaryotes. Biophys J 82:2627–2634
75. Losi A, Kottke T, Hegemann P (2004) Recording of blue light-induced energy and volume changes within the wild-type and mutated phot-LOV1 domain from *Chlamydomonas reinhardtii*. Biophys J 86:1051–1060
76. Salzmann S, Tatchen J, Marian CM (2008) The photophysics of flavins: what makes the difference between gas phase and aqueous solution? J Photochem Photobiol A 198:221–231
77. Salzmann S, Martinez-Junza V, Zorn B, Braslavsky SE, Mansurova M, Marian CM, Gärtner W (2009) Photophysical properties of structurally and electronically modified flavin derivatives determined by spectroscopy and theoretical calculations. J Phys Chem A 113:9365–9375
78. Salzmann S, Silva-Junior MR, Thiel W, Marian CM (2009) Influence of the LOV domain on low-lying excited states of flavin: a combined quantum-mechanics/molecular mechanics investigation. J Phys Chem B 113:15610–15618
79. Nakasako M, Zikihara K, Matsuoka D, Katsura H, Tokutomi S (2008) Structural basis of the LOV1 dimerization of *Arabidopsis* phototropins 1 and 2. J Mol Biol 381:718–733
80. Baeurle SA, Kiselev MG, Makarova ES, Nogovitsin EA (2009) Effect of the counterion behavior on the frictional compressive properties of chondroitin sulfate solutions. Polymer 50:1805–1813